The role of flow features and chemical kinetics on the reaction yield in a T-shaped micro-reactor

Alessandro Mariotti, Matteo Antognoli, Chiara Galletti[1], Roberto Mauri, Maria Vittoria Salvetti, Elisabetta Brunazzi

Dipartimento di Ingegneria Civile e Industriale, University of Pisa, Pisa, Italy

Abstract

The effect of flow regimes on the reaction yield of a chemical reaction occurring in a T-shaped micro-reactor is investigated both experimentally and numerically by spanning different Reynolds and Damköhler numbers. The experimental set-up is arranged in order to get in-line information on both fluid dynamics and reaction progress along the mixing channel. Numerical simulations are performed using mesh-adaption cycles to well resolve the mixing between reactants; in this manner, the agreement between experiments and numerical simulations is very satisfactory. For the considered reaction involving two reagents different from water, despite flow regimes are coherent with the ones observed in case of water mixing, significant differences arise because stratification occurs due to the different density of the fluid streams.

The dependency of reaction yield on both Reynolds and Damköhler numbers is strongly affected by the flow regimes. In the stratified regime, the reaction yield decreases with the Reynolds number, because the reduced residence time hampers the reaction progress, while in the engulfment regime, the Reynolds number has a positive effect on the yield, thanks to the enhanced mixing.

Keywords: T-junction, Computational Fluid Dynamics, Direct Numerical Simulations, Flow visualization, Damköhler number

[1]corresponging author. E-mail address: chiara.galletti@unipi.it

1. Introduction

Micro-reactor technology is gaining increasing interest for a wide range of applications, including the intensification of chemical reactions for pharmaceutical and fine chemical industries [1][2][3]. The main reason for preferring micro-reactors over conventional batch stirred reactors is the excellent control of the operating conditions that micro-devices offer due to the laminar regime and enhanced heat transfer. In particular, micro-reactors work with a well defined residence time (strictly dependent on the flow rate and on the micro-reactor length), which is probably the main factor to be taken into account for the reaction optimization, especially in presence of unstable or short-lived reactive intermediates. Moreover, the superior temperature control, due to the large surface to volume ratio that micro-devices offer, makes possible to handle highly exothermic or dangerous reactions without the need of diluting the reactants, as conversely often required in conventional batch stirred vessels [4] [5]. The above features result in improved yields and selectivities, as well as in the possibility to conduct reactions that are difficult or even impossible to be performed in batch-wise mode, and in the use of operating conditions that allow exploring new chemical pathways. In addition, micro-reactor technology can solve one of the main problems of conventional process design, namely the scale-up of chemical reactors from laboratory to industrial size, by using many microfluidic devices working in parallel (i.e., the so-called numbering up). Therefore, as large volume production can be attained through massive parallelization of the micro-unit processes [6], reactor miniaturization has found many applications in diverse branches of engineering. In particular, the pharmaceutical industry is naturally interested in micro-reactor technology as it reduces the time that is needed to bring a new compound or a new synthesis route from the research

lab to its industrial production stage [7].

Roberge et al. [8] estimated that around 50% of the homogeneous reactions involved in pharmaceutical and fine chemistry industries would benefit from continuous processes in micro-reactors. Among them, we can identify: very fast reactions (i.e. with chemical timescale $\tau_c < 1$ s) which are then controlled by mixing; rapid reactions (i.e, with 1 s $< \tau_c <$ 10 min) which are kinetically controlled but would benefit from the enhanced heat transfer; dangerous reactions. As concerns the former types of reactions, micro-reactors well allow to explore the potentialities of flash chemistry [9], through the conduction of extremely fast reactions in a highly controlled manner to produce desired compounds with high selectivity. Flash chemistry is indeed a novel concept in both organic and sustainable synthesis as its chemical transformations are practically impossible to be conducted using conventional batch conditions.

In this framework, in spite of the above described promising features of micro-reactors, fundamental research is needed to fully characterize and understand their behavior under different operating conditions and, hence, to optimize their design and efficiency. In particular, the efficient mixing of the reactants in such small devices is an issue because the flow is laminar, given the low Reynolds number stemming from the tiny dimensions. Hence, extensive literature can be found on the mixing performances of micro-mixers. In particular, the different flow regimes occurring in T-mixers when increasing Reynolds number have been described in detail and mixing occurring in each regime has been characterized as well (see e.g. [10] for an overview). On the other hand,flow regimes occurring when mixing liquids different from water are less investigated [38]. Also, not much is available concerning the optimization of micro-reactors, despite the fact that the coupling between mixing and chemical reaction has been widely investigated in general [11], [12]. A noticeable exception is the work by [13], [14]

which numerically simulated the reactive mixing in T-shaped micro-reactors through a hybrid numerical approach and pointed out that chemical reactions interact with convective and diffusive transport in a complex way. In particular, they showed that an increase of Reynolds number, although increasing mixing, does not necessarily lead to an improvement of the reaction yield, due to the reduction of the residence time.

The aim of the present work is to further investigate and characterize how the flow features and mixing impact on the reaction yield in a T-shaped micro-reactor, for different reaction rates. To this purpose we use jointly numerical simulations and experiments, which were carried out at different Reynolds and Damköhler numbers, the latter describing the competition between chemical kinetics and flow. This was possible as the chosen chemical reaction is catalyzed by an acid in homogeneous phase, allowing to span different kinetic constants. Moreover, this reaction is characterized by a progressive decolorization of the mixture, as the products form; hence, the reaction yield can be computed by a proper post processing of the experimental visualizations. The analysis is carried out for a T-shaped micro-reactor, whose fluid dynamical performances have been thoroughly characterized when fed with water [15][16][17][10]. Hence, we preliminary discuss the flow features for the present working fluids, highlighting differences and similarities with the flow regimes that have been identified with water. Finally, a semi-empirical scaling of the reaction yield with the Reynolds and Damköhler numbers is proposed in the different regimes.

2. Test case

The test reaction is the methylene blue reduction in which the methylene blue (MB^+, a water-soluble cationic dye molecule) is reduced to the colorless leucomethylene blue (LMB^+, a hydrogenated molecule), using the ascorbic acid

(AsA). The reaction can be catalysed in presence of hydrogen chloride (HCl).

$$\mathrm{MB^+ + AsA \rightarrow LMB^+ + DA}$$

where DA represents the deydroascorbic acid. The reaction kinetics was studied experimentally at room temperature by Mowry and Ogren [18] who suggested the following reaction rate:

$$\frac{d[\mathrm{MB^+}]}{dt} = -\left(k_0 + k_1[\mathrm{HCl}]\right)[\mathrm{AsA}][\mathrm{MB^+}] = -k_r[\mathrm{MB^+}] \tag{1}$$

where $k_0 = 1$ L/mols and $k_1 = 5.3$ L^2/mol^{2}s. The above expression indicates a pseudo-first order reaction in case of an excess of ascorbic acid.

Such reaction was chosen for the present investigation because of the possibility to exploit the decolorization of the blue reactant to visualize the reaction progress and because this reaction has a typical timescale of the order of the residence time in the micro-device (i.e. $\tau_c = 0.1 - 10$ s). In addition, the kinetic constant k_r can be varied by using different concentrations of HCl, thus allowing to span different kinetic conditions.

3. Experiments

3.1. Reactor, experimental set-up and chemicals

The micro-reactor is made of polymethylmethacrylate (PMMA) and consists of three layers, which are sealed with two double-sided adhesive films and screws. The central layer, with a thickness equal to 1 mm, has a T-shaped cutting through. The top and bottom layers, with a thickness of 3 mm each, are equipped with fluidic connections and allow optical access. A picture and a sketch of the T-mixer geometry are shown in Fig. 1, together with the adopted frame of reference. The inlet channels have a square cross-section, with $W_i = H = 1$ mm, while the mixing channel presents a 2:1 aspect ratio, i.e.

$W_o = 2H = 2$ mm, so that its hydraulic diameter is $d = 4H/3$. This quantity will be used in the following text to define non-dimensional coordinates, i.e., $X = x/d$, $Y = y/d$, and $Z = z/d$. The length of the inlet channels, $L_i = 40$ mm $\cong 30d$, is enough to allow a fully developed flow at the confluence, while the length of the mixing channel, $L_o = 60$ mm $\cong 45d$, is enough to allow the complete evolution of vortical structures [15].

[Figure 1 about here.]

The aqueous solution of MB^+ and HCl is fed into one inlet of the T-reactor, while the aqueous solution of AsA enters the other inlet.

The solutions of MB^+ and HCl were prepared by dissolving 17 mg/L of MB^+ powder (by Sigma Aldrich) in aqueous solutions of HCl (by Sigma Aldrich) with different concentrations of HCl. The concentration of MB^+ was thus kept fixed at $[MB^+] = 5.31 \times 10^{-5}$ mol/L, while the HCl concentration was changed in the range of $[HCl] = 0.1 - 2.19$ mol/L. The concentration of ascorbic acid was kept fixed at [AsA] = 1.7 mol/L, and was prepared by dissolving 300 mg/L of L-Ascorbic Acid (Ultrafine Vitamin C-powder by Cutatonic®) in deionized water.

The values of the pseudo-first order kinetic constant k_r obtained for the different HCl concentrations are reported in Table 1.

[Table 1 about here.]

The two streams were introduced at equal flow rates by using a KD Scientific syringe pump Gemini 88, equipped with two Becton Dickson plastic syringes of 60 mL. After each experimental test, the pump is stopped and then started again to reach the desired flow rate for a new test. This was made to avoid any hysteresis in the mixing process.

The flow topology and progress of the reaction at the T-junction and along the mixing channel were observed with an upright microscope (model Eclipse 80i from Nikon, Japan) with a magnifying lens of $4\times$ and an aperture value setting equal to $N.A. = 0.13$. The light source is a D-LH 12V-100W halogen lamp and all the experiments were performed in a dark room in order to maintain a constant level of luminosity and to minimize any reflection and shadow. The images were collected by using the high-speed camera Optomotive Velociraptor HS, having a square monochrome sensor with a resolution of 2048×2048 pixels. The maximum frame rate of the camera is equal to 174 frames/s for the whole sensor, which can be increased by activating only a smaller rectangular portion of the sensor (the frame rate is inversely proportional to the number of pixel in the horizontal direction). Thus, for the investigated flow regimes, a resolution of 920×2048 pixels and a frame rate up to 387 frames/s were chosen. The equivalent dimension of a pixel is 2.6 μm. In front of the camera a $0.5\times$ lens is mounted to collect a region of $1.8d \times 4d$ in a single image. Visualizations were made at the T-junction, in the initial portion of the mixing-channel,and at different locations along the mixing channel.

3.2. Flow topology & reaction yield visualizations

The color-fading reaction was followed by analyzing the images captured by the camera. Among MB^+, HCl and AsA, the only light absorbing species is MB^+. The light emitted from the lamp crosses the specimen and hence the resulting intensity, captured by the camera, depends on the MB^+ concentration. Preliminary calibration runs were performed to assess the relationship between the MB^+ concentration and light absorbance. These were performed by filling the reactor with various sample solutions of known levels of MB^+ concentration (in the range $0 - 6.25 \cdot 10^{-5}$ mol/L), acquiring images for all these solutions and analyzing pixel by pixel the light-intensity image of each set (100 images per

set). Then the relationship of light absorbance with concentration was estimated for every individual pixel in the image. The procedure is the same as the one reported in Mariotti et al. [16][19][20] where a dye was used to investigate the mixing behavior of the T-mixer. The Lambert-Beers linear relationship between the MB^+ concentration and light absorbance was found to hold for the MB^+ case, with our experimental set up and operating conditions. Thus, during the reaction experiments, normalized depth-averaged MB^+ concentration images were derived from the light intensity images by using the following equation applied for each (ij)-th pixel of the images:

$$\frac{ln(I_{blank,ij}) - ln(I_{k,ij})}{ln(I_{blank,ij}) - ln(I_{max,ij})} = \frac{C_{k,ij}}{C_0} \tag{2}$$

where, $I_{k,ij}$ is the instantaneous value of the light intensity, $C_{k,ij}$ is the instantaneous value of the MB^+ concentration, $I_{blank,ij}$ is the value of light intensity acquired when the mixer is full of only the blank solution, and C_0 is the concentration when the mixer is full of the $C_0 = 5.3 \cdot 10^{-5}$ mol/L MB^+ solution. The acquisition of the references, $I_{blank,ij}$ and $I_{max,ij}$ (light intensity of the blank solution, i.e. the solution with zero MB^+ content, and of the solution with the highest MB^+ concentration, respectively), was necessary for each set of experiments before using the two streams together. In order to limit the uncertainty related to time fluctuation of pixel intensity, the references $I_{blank,ij}$ and $I_{max,ij}$ are chosen to be their arithmetic mean values over 80 frames each. For the computation of $I_{k,ij}$, during the reaction experiments, 600 images with a frame rate of 387 frames/s were acquired for each Re step. An off-line automatized procedure was developed to post-process the images, so that pixel intensity maps were directly converted into distributions of normalized depth-averaged MB^+ concentration.

The refractive index of the two streams differs a little (about 1.33 for the

MB^+ solution, compared to $1.36 - 1.37$ for the ascorbic acid solution, [21]). Therefore, the optical rays are somewhat diverted in their course across the specimen due to refraction resulting from the refractive index differences between the two solutions. Consequently, at the contact fronts of the two different fluids, darker or brighter streaks compared to the rest of the image, can be observed. Proper focusing of the condenser (with regard to height in relation to the objective) and aperture adjustments of the condenser and the field diaphragms, allowed us to either minimize the presence of streaks in the collected images (that would otherwise offset the concentration measurement during the reaction yield visualizations), or instead deliberately highlight the streaks; in this way streaks are exploited to visualize the flow topology and vortical structures.

4. Numerical model

The flow is incompressible and, in the considered range of Reynolds numbers, it is also steady. The problem can thus be described by the Navier-Stokes together with transport/reaction equations for all chemical species except water (i.e, for MB^+, HCl, AsA, LMB^+ and DA), written in the following in non-dimensional form:

$$\nabla \cdot \mathbf{u} = 0 \tag{3}$$

$$\mathbf{u} \cdot \nabla \mathbf{u} = -\nabla P + \frac{1}{Re} \nabla^2 \mathbf{u} + \frac{1}{Fr} \hat{\mathbf{g}} \tag{4}$$

$$\mathbf{u} \cdot \nabla Y_k = \frac{1}{Pe} \nabla^2 Y_k + \frac{d}{\rho U} \dot{\omega}_k \tag{5}$$

where length and velocities are normalized with the mixing channel hydraulic diameter d and the inlet bulk velocity U. P is the modified non-dimensional

pressure and $\hat{\mathbf{g}}$ is the non-dimensional gravity, i.e. $\hat{\mathbf{g}} = \frac{\mathbf{g}}{g}$. Re is the Reynolds number, $Re = \frac{\rho U d}{\nu}$, where ρ is the density and ν is the dynamic viscosity. Fr is the Froude number, i.e. $Fr = \frac{gd}{U^2}$, and Pe is the Peclet number, i.e $Pe = \frac{Ud}{\mathcal{D}}$, where $\mathcal{D}$ is the molecular diffusivity. Y_k is the mass fraction of the k-th chemical species, while $\dot{\omega}_k$ represents its rate of consumption or production due to chemical reactions. The presence of the acid catalyst was implemented in the code by using two parallel reactions, i.e.:

$$\mathrm{MB^+ + AsA} \xrightarrow{k_0} \mathrm{LMB^+ + DA}$$
$$\mathrm{MB^+ + AsA + HCl} \xrightarrow{k_1} \mathrm{LMB^+ + DA + HCl}$$

where all chemical species are in aqueous solution. Accordingly, the source term for the k^{th} chemical species is $\dot{\omega}_k = \sum_{i=0,1} \nu_{k,i} k_i \prod_{j=1,5} (\rho Y_j)^{\nu_{j,i}}$, where k_i is the kinetic constant of the i^{th} reaction, $\nu_{k,i}$ is the stoichiometric coefficient of the k^{th} chemical species in the i^{th} reaction and $\nu_{j,i}$ is the order of the i^{th} reaction with respect to the j^{th} chemical species.

We can also define a Damköhler number for each species, Da_k, as the ratio between the formation or destruction rate and the convective flux along the mixing channel, i.e. $Da_k = L_o \dot{\omega}_k / U \rho Y_k$. In particular, according to this definition, the conservation equation for the methylene blue can be rearranged as follows:

$$\mathbf{u} \cdot \nabla Y_{MB^+} = \frac{1}{Pe} \nabla^2 Y_{MB^+} + \frac{d}{L_0} Da Y_{MB^+} \tag{6}$$

In the above equation the Damköhler number is estimated using the reaction rate of the methylene blue, thus leading to $Da_k = L_o \dot{\omega}_{MB^+} / U \rho Y_{MB^+} = L_o k_r / U$ according to the pseudo-first order reaction rate defined in Eq. (1). The viscosity μ and density ρ of the liquid mixture are both taken to be a function of the ascorbic acid concentration as follows:

$$\mu = \mu_o \left(1 + 1.0605 Y_{AsA} + 5.7219 Y_{AsA}^2\right) \tag{7}$$

$$\rho = \rho_0 \left(1 + 0.39070 Y_{AsA} + 0.1617 Y_{AsA}^2\right) \tag{8}$$

where μ_0 and ρ_0 are the density and the viscosity of water at 20°C, as the properties of the MB^+ acidic solutions are assumed to be close to those of water[22]. It is worth noting that the effect of the ascorbic acid on the physical properties is not negligible. The density and viscosity of the aqueous stream of ascorbic acid entering one inlet channel are approximately 1.117 and 1.7 times larger than those of the MB^+/HCl aqueous solution, respectively, i.e. $\frac{\rho}{\rho_o} = 1.117$ and $\frac{\mu}{\mu_o} = 1.7$.

The above set of equations was discretized using ANSYS Fluent, which is based on the finite volume method. In our recent works, the performance of this code was successfully tested against both experiments [16] and a spectral element code [23] for the prediction of the mixing process in the same T-shaped micro-reactor.

A steady solver with a second order upwind interpolation scheme was used along with the SIMPLE algorithm for the pressure-velocity coupling [23]. Convergence was assessed by monitoring the MB^+ concentration in four locations along the mixing channel as well as by checking the steadiness of residuals with iterations. In specific, at convergence normalized residuals were all below 10^{-9}. As for the boundary conditions, no-slip velocity is set at the channel walls, while uniform velocity and concentration is imposed at the entrance, as the inlet channels are long enough to provide a fully developed flow at the T confluence. A pressure outlet condition with ambient pressure is given at the exit of the mixing channel.

The starting computational grid is fully structured with 4.7M cells. The cells are cubical at the confluence region, whereas they elongate towards the inlets and outlet. Details on the grid independence study, carried out in non-reactive

conditions, may be found in previous works [16] [23]. This starting grid was also adapted and refined in regions of high reaction rates, in order to better capture the mixing of reactants. The importance of mesh adaptation in the numerical simulation of micro-reactors was als pointed out in previous works (see e.g. [24] [25]). The grid refinement is carried out herein by using sequential adaption cycles. In each cycle, the cells in which the reaction rate is higher than a given threshold are identified and the additional cells are created locally by dividing in two parts each edge of the previously marked cells. Typically, three cycles were sufficient to get results which were independent of further refinements. After the mesh adaption, the number of cells was usually in the range of $10 - 12$M. Figure 2 compares the original (on the left) and the adapted grid (on the right) showing details in the confluence region of the T-shaped micro-reactor. Colors correspond to the reaction rate of MB^+.

[Figure 2 about here.]

5. Results

5.1. Flow regimes and mixing

Since the HCl concentration has a negligible influence on the flow patterns for the investigated range of compositions, as the mixture properties depend mainly on the ascorbic acid content, which was kept fixed in all the three considered cases, the different flow regimes will be analyzed showing their features only for the case with an acid concentration [HCl] = 1.00 mol/L (i.e. test n.2 of Table 1).

Figs. 3a-d show experimental flow visualizations for $Re = 10-60$, while Figs. 3e-h the corresponding experimental concentration of MB^+ averaged over the reactor depth and, finally, Figs. 3i-l the MB^+ concentration obtained in numerical simulations in different cross-sections of the mixing channel for $-20 \leq Y \leq -0.5$

(this last information is not available in experiments). The MB^+ concentration is reported herein and in the following of the paper in non-dimensional form, being 1 the non-dimensional concentration when the mixer is full of the MB^+ solution. The Reynolds numbers of Fig. 3 correspond to the so-called segregated regime, in which the two streams remain segregated and mixing occurs only by diffusion at the interface. Compared to the case of a T-mixer operating with a single fluid, in which the two streams flow side by side in the mixing channel and the interface is parallel to the side walls of the mixing channel (see e.g. [10]), stratification occurs in the present case due to the higher density of the aqueous solution of ascorbic acid. Indeed, it can be seen from Figs. 3i-l that the aqueous solution of ascorbic acid (white stream, incoming from the right) moves towards the bottom of the microdevice while the methylene blue aqueous solution (shown as black on the cross-section and light grey in the rest of the device, entering the mixing channel from the left) tends to occupy the upper part of the channel. The lower is the Reynolds number, and, thus the mean convective velocity, the more upstream stratification occurs in the mixing channel. As a consequence, when visualizing the MB^+ concentration averaged over the microdevice depth, as in Figs. 3e-h, the two streams appear as they were almost perfectly mixed in the mixing channel, but this is only the effect of the previously discussed stratification. Figs. 3e-h also confirm how the stratification occurs more downstream in the mixing channel as the Reynolds number is increased. Finally, it is interesting to note how the streaks, originating from optical rays refraction, in Figs. 3a-d help in identifying the interface between the two streams. For instance, the two semi-elliptical dark lines, one for each inlet, appearing in all Figs. 3a-d, which originate from refraction of the optical rays crossing media with different fluid density and refraction index, separate the inlet regions, where just one fluid is present, from the outlet channel in which

the refraction index changes, because the two fluid streams come into contact and stratify (compare also with panels e-h). At $Re = 60$ a longitudinal streak is also observed in the experimental image (see Fig. 3d) in correspondence of the vertical mid-plane in the upper part of the mixing channel; it identifies the interface between the two streams, which at this Re remains almost vertical in the first part of the mixing channel (see Fig. 3l).

[Figure 3 about here.]

At larger Reynolds numbers the flow undergoes a change in flow topology with the onset of the so-called *vortex* regime, which is characterized by the presence of vortical structures in the mixing channel. This regime has been largely investigated in case of water mixing (see, for instance, [26], [27], [28], [29], [30], [31], [32], [10]). In particular it has been found that this regime exhibits the presence of two U-shaped vortical structures, whose top parts are located at the confluence of the two inlet streams, and stem from two flow recirculation regions formed near the top wall. The legs of the U-shaped structures are counter-rotating and develop in the mixing channel. In case of devices operating with a single fluid, these vortical structures are perfectly symmetric, thus leading to a flow field which is characterized by two reflectional symmetries. As a result, also in this regime mixing occurs only by diffusion and, hence, remains quite low. The flow visualizations obtained for the present case in the vortex regime are shown in Figs. 4a-c for $Re = 80$, 100 and 120. The corresponding vortical structures, as identified from the numerical simulations through the λ_2 criterion [33], are reported in Figs. 4d-f. As in the case of devices operating with a single fluid, the presence of two U-shaped vortical structures having a head which is almost perpendicular to the inlet streams, can be observed. However, the intensity of the vortical structures in the mixing channel is not equal in the two sides due to the different density and viscosity of the two fluid streams; this can be seen,

for instance, in the different length of the vortex legs in Fig. 4d. Therefore, one of the two reflectional symmetries is lost. This leads to a noticeable although small effect of the velocity induced by the 3D vortical structures on the mixing between the two streams, as it can be seen, for instance, in Figs. 4g-i, reporting the MB^+ concentration obtained in numerical simulations in different cross-sections of the mixing channel for $-20 \leq Y \leq -0.5$. Indeed, the interface in the first part of the mixing channel, where stratification is not yet completed, takes a more wavy shape, due to the signature of the vortical structures present in the channel. Once again, complete stratification of the streams occurs more upstream for lower Re.

[Figure 4 about here.]

By further increasing the Reynolds number, the flow undergoes the so-called *engulfment* regime which has been extensively characterized in case of single-fluid mixing (see, for instance, [16] [26] [30] [29] [32] [34][35] [10]) as this regime has a practical interest because it strongly enhances mixing. A key role is played by the recirculation regions at the confluence of the inlet streams, leading to a tilting of the top parts of the U-shaped vortical structures, thus resulting in a loss of the double reflectional symmetry as one of the two legs of each vortical structure is more fed by the incoming fluid than the other. As a result, only the two strongest legs, which are co-rotating, survive further away in the mixing channel, while the two weakest legs rapidly vanish. The two co-rotating vortices enable mixing through convection and produce S-shaped flow patterns in cross-sections of the mixing channel, with each inlet fluid stream being able to reach the opposite wall. The experimental images as well as the vortical structures and the MB^+ concentration at different cross-sections obtained in numerical simulations for the present case in the engulfment regime (Re = 150, 180, 230 and 280) are reported in Fig. 5.

[Figure 5 about here.]

The flow features are similar to those of the single-fluid mixing case described above, with a tilting of the top head of the U-shaped vortical structures and a consequent loss of symmetry of the vortical legs. The two strongest vortical legs survive in the mixing channel, while the weakest legs soon disappear. As previously observed, in contrast to the single-fluid mixing case, here the intensities of the two weak and of the two strong legs are different from each other, due to the different properties of the inlet fluids. The tilting angle of the U-shaped structures augments with increasing Reynolds number from $Re = 150$ to $Re = 280$ (compare for instance Fig. 5e and Fig. 5h), with a consequent more pronounced asymmetry of the vortical legs. Moreover, for large Reynolds numbers, i.e. $Re = 230$ and $Re = 280$, the strongest co-rotating vortical legs in the mixing channel are swirled. Note how, especially at the largest Reynolds numbers (see, e.g. Figs. 5b-d), the streaks in the experimental visualizations identify the signatures of the co-rotating vortical structures in the mixing channel and of their swirling as well as those of the top parts of these structures near the device top wall. The effects of the two-rotating vortical structures in improving the mixing between the two streams, which are pushed towards the opposite wall, is clearly visible in Figs. 5i-l. Some stratification effects are present, since the aqueous solution of ascorbic acid (white color) tends to move towards the bottom of the mixing channel more than that of methylene blue (dark). However, stratification is less important than in the segregated and vortical regime, since here convective effects dominate.

Further increasing the Re number, the flow becomes unsteady and time-periodic. This unsteady flow has been characterized both experimentally and numerically in case of water mixing, pointing out the presence of two topological flow patterns, i.e. the *unsteady asymmetric* and subsequently the *unsteady*

symmetric regimes, the latter showing a strong degree of symmetry which hampers the mixing process (see for example [36],[37] [16],[17]). These unsteady regimes will not be analyzed here, but both of them were found to occur also in the present reactive case. The *unsteady asymmetric* regime was found for $Re = 320 - 450$, whereas the *unsteady symmetric* regime occurred in the range $Re = 500 - 650$.

Thus, summarizing, in the present reactive cases, the same flow regimes as in devices working with a single fluid are observed when increasing Reynolds number; their features are also very similar to those of the single-fluid case, the only differences are due to stratification depending mainly on the ascorbic acid content. Since, it was kept fixed in all the three cases considered herein, the previously described flow features apply to all the reaction rates that will be analyzed in the following.

In the case of a single fluid, the mixing in the different regimes has been quantified in the literature by using different possible indicators (see [10]). We consider herein the degree of mixing, δ_m, defined as in [38]. Fig. 6 shows δ_m as a function of the Reynolds number for the device operating with water. It is compared with the degree of mixing numerically estimated for the present working fluids, by running numerical simulations with a negligible k_r (i.e. $k_r = 0.01 s^{-1}$) and thus letting the methylene blue behave as a dye, i.e. a passive tracer; this in order to avoid any ambiguity in the computation of δ_m due to the presence of reaction products. It is worth noting that the graph does not show a steep increase of the degree of mixing at the onset of the engulfment regime as observed for the water mixing case, as some degree of mixing is present also in the vortex regime. This is due to the stratification of the two streams which leads to an increase of the mixing because of the loss of symmetry occurring already in this regime. However, also in the present case it is clear that the

degree of mixing in the engulfment regime ($Re \geq 150$) is significantly higher than in the other ones.

[Figure 6 about here.]

5.2. Validation

In the previous Sec. 5.1, the flow and mixing characteristics with varying Reynolds numbers have been described by using experimental and numerical results. Sec. 5.1 also shows that there is a very good qualitative agreement between experiments and simulations. Before analyzing the behavior of the reaction yield in the different flow regimes, a quantitative comparison between experiments and simulations is provided herein. To this aim, numerical results were post-processed to determine the depth-averaged concentration of the methylene blue.

Fig. 7 compares the experimental and numerical profiles along the x coordinate of the depth-averaged concentration of the methylene blue at $Re = 30$ and [HCl] = 1.00 mol/L. The top panels show the corresponding concentration over the considered cross-section, for the sake of clarity. It can be seen that the quantitative agreement between experiments and predictions is very satisfactory. The same comparisons have been made for different Reynolds numbers and for all the three considered concentrations of HCl; in all cases the agreement is very good (not shown here for the sake of brevity).

[Figure 7 about here.]

In order to give an idea of the effects of grid refinement, Table 2 shows the average of the methylene blue concentration over the cross-section at $Y = -25$ obtained in numerical simulations with different levels of grid refinement for three Reynolds numbers in the previously described regimes, together with the corresponding values measured in experiments. Grid independences was reached

when differences on the non-dimensional average MB+ concentration at the $Y = -25$ cross-section are below 1% for all the considered Reynolds numbers. It can be seen that grid independence is reached at the third grid refinement as well as an excellent agreement with the experiments.

[Table 2 about here.]

5.3. Reaction yield

The reaction progress can be monitored by looking at the evolution over the mixing channel axis of the methylene blue concentration averaged over the corresponding cross-section; we remind that as the reaction progresses the concentration of methylene blue decreases. Numerical and experimental results are shown in Fig. 8 for the three [HCl] concentrations, corresponding to different reaction rates, k_r, and are divided according to the flow regime.

[Figure 8 about here.]

First of all, note the very good agreement between the numerical results and the experiments. The experimental error bars were computed using the following relationship:

$$err = \frac{2\sigma}{\sqrt{N-1}} \tag{9}$$

where N is equal to the number of realizations of the same measurement (in the present work $N = 600$ and σ indicates the root mean square deviation).

Let us analyze, then, the behavior in the different regimes. In the stratified regime (Figs. 8a-c), the methylene blue concentration decreases more slowly along the mixing channel with increasing Re, for all the investigated k_r, thus indicating a reduction of the reaction progress. This can be explained by considering that in the stratified regime, the contact area between the two streams is scarcely affected by the velocity; however, the residence time diminishes with

increasing Re leading to a reduction of the reaction progress and thus to an increase of the final methylene blue concentration. As for the effect of the kinetic constant k_r, its increase leads to a faster reaction and hence to a lower methylene blue concentration at the outlet of the mixing channel for a given Reynolds number.

In contrast, in the vortex regime (see Figs. 8d-f) the MB^+ concentration decreases faster along the mixing channel axis with increasing the Reynolds number. Indeed, in such regime the Reynolds number affects the strength of the vortical structures and thus has a positive effect on the contact area between the two reactant streams. Such positive effect overcomes the negative effect of Re on the residence time, ultimately leading to an improvement of the reaction progress.

Finally, the engulfment regime (see Figs. 8g-i) is the one which provides, as expected, the largest decrease of methylene blue concentration and thus the highest reaction yields. As in the vortex regime, an increase of Re enhances the contact area between the two fluid streams and thus improves the reaction yield, as confirmed by the reduction of methylene blue concentration.

As an example, Fig. 9 shows the region of high reaction rates for the three regimes, highlighting the effect of the vortical structures on the contact area between the two streams in both vortex and engulfment regimes.

[Figure 9 about here.]

In order to quantitatively estimate the reaction yield, the concentration of methylene blue averaged over the $Y = -25$ cross-section of the microdevice (near the mixing channel outlet) was used. More precisely, the reaction yield, η, is defined as follows:

$$\eta = 1 - 2\frac{C_{BM^+,out}}{C_{BM^+,in}} \tag{10}$$

where $C_{BM^+,out}$ and $C_{BM^+,in}$ are the average methylene blue concentrations at $Y = -25$ and at device inlet, respectively. Experimental and numerically predicted yields as a function of the Reynolds number are reported in Fig. 10a for all the considered reaction rates.

[Figure 10 about here.]

Once again, in all cases, the correspondence between experimental and predicted yields is very satisfactory. In agreement to what observed from Fig. 8, two different trends are visible: for $Re \leq 60$ (segregated regime), the reaction yield decreases with Reynolds, while for larger Reynolds (vortex and engulfment regimes) η increases with increasing Re. As discussed above, the non-monotonic behavior of η with Reynolds is due to the interplay between the contact area of the two streams and the residence time and on how they vary with Reynolds. As previously said, in the segregated regime the contact area is scarcely affected by Re so that the negative effect of increasing Re on the residence time prevails, hence leading to a reduction of the reaction yield. In contrast, in both vortex and engulfment regimes, the remarkable effect of Re on the contact area and on the mixing of reactants dominates over the change of the residence time, ultimately resulting in a reaction enhancement. It is also interesting to remark that the slope of η vs. Re varies with k_r in all regimes.

Based on the previous considerations, we can assume that the reaction yield η depends on the kinetic constant k_r, on the degree of mixing δ_m, which is in turn connected with the contact area between the two streams, as well as on the residence time τ in the mixing channel. Since we observed that the flow and mixing features are independent of HCl concentration, we can also reasonably assume that the effects of k_r on the degree of mixing are negligible and, hence, the degree of mixing depends solely on the Reynolds number. Hence, we can

write:

$$\eta \propto \widetilde{k_r}^{\alpha} Re^{\beta} \tag{11}$$

where $\widetilde{k_r}$ is a non dimensional kinetic constant, i.e. $\widetilde{k_r} = k_r \frac{L_o d_h}{\nu}$. The above expression can be also written as a function of the Damköhler number, representing the residence to chemical time scale ratio, i.e. $Da = L_o k_r / U = \widetilde{k_r} / Re$ (see also Sec. 4), thus leading to:

$$\eta \propto \frac{\widetilde{k_r}^{\alpha+\beta}}{Da^{\beta}} \tag{12}$$

The reaction yield is also reported as a function of the Damköhler number for all the investigated cases in Fig. 10b. For the sake of clarity, since the range of variation of Da is huge, the Da axis is in logarithmic scale. It can be seen that for large Da, i.e. for low Reynolds numbers corresponding to the segregated regime, the yield values, independently of k_r, all follows the same trend with Da. Indeed, in the segregated regime, for low Re and large Da, the fitting of the yield values shown in Fig. 10 leads to $\alpha = 0.3$ and $\beta = -0.3$ and thus to the following relationship:

$$\eta \propto \frac{\widetilde{k_r}^{0.3}}{Re^{0.3}} \propto \widetilde{Da}^{0.3} \tag{13}$$

Consistently with the previous observations and considerations, in this regime the reaction yield decreases with increasing Re and with increasing Da and when the dependence on Da is considered, there is no explicit dependency on k_r. Indeed, the above relationship is reported by a solid line in Fig. 10b and we can observe that all yield values in the segregated regime well lie on this curve despite they refer to different k_r. This confirms that the mechanism controlling the reaction yield is indeed the ratio between the residence time and the chemical

characteristic time.

In the engulfment regime, i.e. for large Re and low Da, instead, we obtain $\alpha = 0.5$ and $\beta = 0.4$ and thus:

$$\eta \propto \widetilde{k_r}^{0.5} Re^{0.4} \propto \frac{\widetilde{k_r}^{0.1}}{Da^{0.4}} \tag{14}$$

In this regime the reaction yield increases with Re due to the enhanced mixing due to the vortical structures. The effect of the kinetic constant k_r on the yield (i.e. $\eta \propto \widetilde{k_r}^{0.5}$) is larger than the one in the segregated regime as here mixing is strong and thus kinetics plays a more significant role than for small mixing. For instance, the maximum yield was of only 15% for $k_r = 2.60$ 1/s (i.e., for [HCl] = 0.10 mol/L), while it increases up to about 45% for $k_r = 21.43$ 1/s (i.e., for [HCl] = 2.19 mol/L).

6. Conclusions and discussion

The impact of flow features and mixing on the reaction yield in a micro-reactor has been investigated, for different Reynolds numbers and kinetic constants. Joint experimental and numerical investigations have been carried out, which allowed mutual validation, while taking advantage of the details on the flow, mixing and reaction given by numerical simulations.

We considered a T-shaped micromixer, where the two inlet fluids consist of aqueous solutions of a blue dye and of ascorbic acid, that react with one another, forming a colorless product. The flow regimes have been found to be very similar to those well documented in the literature for T-shaped micro-devices operating with a single fluid, except for effects of stratification due to the higher density of the aqueous solution of ascorbic acid. Since the concentration of ascorbic acid was kept fixed in all the three cases considered herein, the flow features are the same for these cases. More in detail, at low Reynolds numbers, the two

streams remain segregated with the aqueous solution of ascorbic acid stratifying on the bottom of the mixing channel. In this regime, mixing occurs only by diffusion and it is, thus, very low. By increasing the Reynolds number, 3D vortical structures form leading to four counter-rotating vortices in the mixing channel. In the single-fluid case, the flow and the vortical structures satisfy the two reflectional symmetries of the geometry. In the present case, the intensity of the vortical structures in the mixing channel is not equal in the two sides due to the different density and viscosity of the two fluid streams; therefore, one of the two reflectional symmetries is lost. This implies a noticeable increase of mixing in this regime compared to the single-fluid case. Finally, for further increased Re, in the engulfment regime, all flow symmetries are broken and only two co-rotating vortical structures survive in the mixing channel, whose induced velocity largely increases mixing compared to the previous regimes. The engulfment flow features and mixing performances for the present case are very similar to those of devices operating with a single fluid, with only small effects of flow stratification.

The progress of the reaction has been monitored experimentally and numerically through the evolution of the averaged concentration of methylene blue along the mixing channel and the reaction yield has been evaluated near the outlet of the device. The flow and mixing features have a dramatic impact on the reaction progress and yield. Indeed, two opposite trends with Re are observed in the segregated regime compared to the vortex and engulfment ones, independently of the kinetic constant. In the segregated regime, the reaction yield is found to decrease with increasing Re. This happens because mixing occurs mainly by molecular diffusion, with a contact area between the two streams which is only slightly dependent on the inlet velocity, and, thus, on Re. Hence, an increase of velocity leads to a decrease of the reaction yield because the re-

duced residence time limits the reaction progress. This is also confirmed by the fact that the reaction yield behavior is found to be fitted by $Da^{0.3}$ without any explicit dependency on k_r. This means that the residence to chemical time-scale ratio is the key factor dominating the reaction rate in this regime. Conversely, in the vortex and engulfment regimes the yield increases with Re because, increasing Re, the contact area between the two streams becomes larger and mixing more efficient. In particular, the reaction yield in the engulfment regime is found to be $\eta \propto \widetilde{k_r}^{0.5} Re^{0.4}$. Thus, the gain in efficiency due to better mixing increases for larger kinetic constants.

Summarizing, the present results confirm that the studies of the flow features and mixing performances, carried out for devices operating with a single fluid and in non-reactive conditions, provide significant information to optimize the reaction yield in micro-reactors. In particular, in the engulfment regime the reaction progress is enhanced because of the mixing induced by the 3D vorticity system, molecular diffusion becoming negligible, and this leads to a remarkable increase of the reaction yield. This behavior was observed for all investigated kinetic constants, although, from a quantitative viewpoint, the yield gain with increasing Re is larger for higher k_r.

Acknowledgments

This work was supported by the University of Pisa through the "Progetti di Ricerca di Ateneo PRA 2017-2018" funding program. The authors wish also to thank CINECA computing center (Bologna, Italy) for allowance of computational resources under ISCRA program (class B project "MIRE"). Moreover the authors are grateful to Annamaria Mastromarino and Cesare Merello.

References

[1] I. Rossetti, M. Compagnoni, Chemical reaction engineering, process design and scale-up issues at the frontier of synthesis: Flow chemistry, Chemical Engineering Journal 296 (2016) 56–70.

[2] T. Van Gerven, A. Stankiewicz, Structure, energy, synergy, time-the fundamentals of process intensification, Industrial & Engineering Chemistry Research 48 (2009) 2465–2474.

[3] R. Gani, J. Badyga, B. Biscans, E. Brunazzi, J.-C. Charpentier, E. Drioli, H. Feise, A. Furlong, K. M. V. Geem, J.-C. de Hemptinne, A. J. ten Kate, G. M. Kontogeorgis, F. Manenti, G. B. Marin, S. S. Mansouri, P. M. Piccione, A. Povoa, M. A. Rodrigo, B. Sarup, E. Sorensen, I. A. Udugama, J. M. Woodley, A multi-layered view of chemical and biochemical engineering, Chemical Engineering Research and Design 155 (2020) 133 – 145.

[4] F. Fanelli, G. Parisi, L. Degennaro, R. Luisi, Contribution of microreactor technology and flow chemistry to the development of green and sustainable synthesis, Beilstein Journal of Organic Chemistry 13 (2017) 520–542.

[5] S. Löbbecke, J. Antes, W. Ferstl, D. Boskovic, T. Türcke, M. Schwarzer, H. Krause, Microreactors for processing of hazardous and explosible reactions, in: IChemE (Ed.), IChemE Symposium Series No. 153: Proceed. 12th International Symposium Loss Prevention and Safety Promotion in the Process Industries, Edinburgh, UK, 22., 2007.

[6] F. H. Kriel, S. Woollam, R. J. Gordon, R. A. Grant, C. Priest, Numbering-up yy microfluidic chips for higher-throughput solvent extraction of platinum(iv) chloride, Microfluidics and Nanofluidics 20 (2016) 1–7.

[7] P. Watts, C. Wiles, Recent advances in synthetic micro reaction technology, Chemical Communications (2007) 443–467.

[8] D. M. Roberge, L. Ducry, N. Bieler, P. Cretton, B. Zimmermann, Microreactor technology: A revolution for the fine chemical and pharmaceutical industries?, Chemical Engineering & Technology 28 (2005) 318–323.

[9] J.-I. Yoshida, Y. Takahashi, A. Nagaki, Flash chemistry: flow chemistry that cannot be done in batch, Chemical Communications 49 (2013) 9896–9904.

[10] S. Camarri, A. Mariotti, C. Galletti, E. Brunazzi, R. Mauri, M. V. Salvetti, An overview of flow features and mixing in micro T and arrow mixers, Industrial & Engineering Chemistry Research 59 (2020) 3669–3686.

[11] S. I. A. Shah, L. W. Kostiuk, S. M. Kresta, Mixing, reaction rates, and stoichiometry on yield for mixing sensitive reactions - part I: Model development, International Journal of Chemical Engineering (2012) 750162.

[12] S. I. A. Shah, L. W. Kostiuk, S. M. Kresta, Mixing, reaction rates, and stoichiometry on yield for mixing sensitive reactions - part II: Design protocols, International Journal of Chemical Engineering (2012) 654321.

[13] D. Bothe, A. Lojewski, H.-J. Warnecke, Fully resolved numerical simulation of reactive mixing in a T-shaped micromixer using parabolized species equations, Chemical Engineering Science 66 (2011) 6424–6440.

[14] D. Bothe, A. Lojewski, H.-J. Warnecke, Computational analysis of an instantaneous chemical reaction in a T-microreactor, AIChE Journal 56 (2010) 1406–1415.

[15] T. Andreussi, C. Galletti, R. Mauri, S. Camarri, M. V. Salvetti, Flow

regimes in T-shaped micro-mixers, Computers and Chemical Engineering 76 (2015) 150–159.

[16] A. Mariotti, C. Galletti, R. Mauri, M. V. Salvetti, E. Brunazzi, Steady and unsteady regimes in a T-shaped micro-mixer: synergic experimental and numerical investigation, Chemical Engineering Journal 341 (2018) 414–431.

[17] A. Mariotti, C. Galletti, M. Salvetti, E. Brunazzi, Unsteady flow regimes in a t-shaped micromixer: Mixing and characteristic frequencies, Industrial and Engineering Chemistry Research 58 (2019) 13340–13356.

[18] S. Mowry, P. J. Ogren, Kinetics of methylene blue reduction by ascorbic acid, Journal of Chemical Education 76 (1999) 970–973.

[19] A. Mariotti, C. Galletti, E. Brunazzi, M. Salvetti, Steady flow regimes and mixing performance in arrow-shaped micro-mixers, Physical Review Fluids 4 (2019) 034201.

[20] M. Salvetti, A. Mariotti, C. Galletti, E. Brunazzi, Steady and unsteady regimes in a T-shaped micro-mixer: Synergic experimental and numerical investigation, in Proceedings of the ASME 2018 5th Joint US-European Fluids Engineering Division Summer Meeting, FEDSM2018 July 15-20, 2018, Montreal, Quebec, Canada, Publisher: American Society of Mechanical Engineers, Fluids Engineering Division, Code 141102 3 (2018).

[21] M. Shamim, S. Khoo, Some physical properties of aqueous l-ascorbic acid solutions, Australian Journal of Chemistry 32 (1979) 2293–2295.

[22] E. Nishikata, T. Ishii, T. Ohta, Viscosities of aqueous hydrochloric acid solutions, and densities and viscosities of aqueous hydroiodic acid solutions, Journal of Chemical & Engineering Data 26 (1981) 254–256.

[23] C. Galletti, A. Mariotti, L. Siconolfi, R. Mauri, E. Brunazzi, Numerical investigation of flow regimes in T-shaped micromixers: benchmark between finite volume and spectral element methods, Canadian Journal of Chemical Engineering 97 (2019) 528–541.

[24] J. Ortega-Casanova, Application of CFD on the optimization by response surface methodology of a micromixing unit and its use as a chemical microreactor, Chemical Engineering and Processing: Process Intensification 117 (2017) 18 – 26.

[25] O. Mierka, M. Munir, C. Spille, J. Timmermann, M. Schlter, S. Turek, Reactive liquid-flow simulation of micromixers based on grid deformation techniques, Chemical Engineering & Technology 40 (2017) 1408–1417.

[26] N. Kockmann, M. Engler, P. Woias, Convective mixing and chemical reactions in t-shaped micro reactors, AIChE Annual Meeting, Conference Proceedings, 2004, pp. 5973–5982.

[27] M. Engler, N. Kockmann, T. Kiefer, P. Woias, Numerical and experimental investigations on liquid mixing in static micromixers, Chemical Engineering Journal 101 (2004) 315–322.

[28] S. Wong, M. Ward, C. Wharton, Micro T-mixer as a rapid mixing micromixer, Sensors and Actuators, B: Chemical 100 (2004) 359–379.

[29] D. Bothe, C. Stemich, H.-J. Warnecke, Mixing in a T-shaped microreactor: scales and quality of mixing, in: W. Marquardt, C. Pantelides (Eds.), 16th European Symposium on Computer Aided Process Engineering and 9th International Symposium on Process Systems Engineering, volume 21 of *Computer Aided Chemical Engineering*, Elsevier, 2006, pp. 351 – 357.

[30] J. Hussong, R. Lindken, M. Pourquie, J. Westerweel, Numerical study

on the flow physics of a t-shaped micro mixer, in: M. Ellero, X. Hu, J. Fröhlich, N. Adams (Eds.), IUTAM Symposium on Advances in Micro- and Nanofluidics, Springer Netherlands, Dordrecht, 2009, pp. 191–205.

[31] A. V. Minakov, V. Y. Rudyak, A. A. Gavrilov, A. A. Dekterev, Mixing in a T-shaped micromixer at moderate Reynolds numbers, Thermophysics and Aeromechanics 19 (2012) 385–395.

[32] A. Fani, S. Camarri, M. V. Salvetti, Investigation of the steady engulfment regime in a three-dimensional T-mixer, Physics of Fluids 25 (2013) 064102.

[33] J. Jeong, F. Hussain, On the identification of a vortex, Journal of Fluid Mechanics 285 (1995) 69–94.

[34] M. Hoffmann, M. Schlter, N. Rbiger, Microscale Flow Visualization, John Wiley & Sons, Ltd, 2013, pp. 93–115.

[35] A. Mariotti, M. Lanzetta, G. Dini, A. Rossi, E. Brunazzi, R. Mauri, C. Galletti, Influence of cross-sectional geometry on mixing in a T-shaped micro-junction, Chemical Engineering Transactions 74 (2019) 955–960.

[36] S. Dreher, N. Kockmann, P. Woias, Characterization of laminar transient flow regimes and mixing in T-shaped micromixers, Heat Transfer Engineering 30 (2009) 91–100.

[37] S. Thomas, T. Ameel, An experimental investigation of moderate reynolds number flow in a T-channel, Experiments in Fluids 49 (2010) 1231–1245.

[38] C. Galletti, G. Arcolini, E. Brunazzi, R. Mauri, Mixing of binary fluids with composition-dependent viscosity in a T-shaped micro-device, Chemical Engineering Science 123 (2015) 300–310.

List of Figures

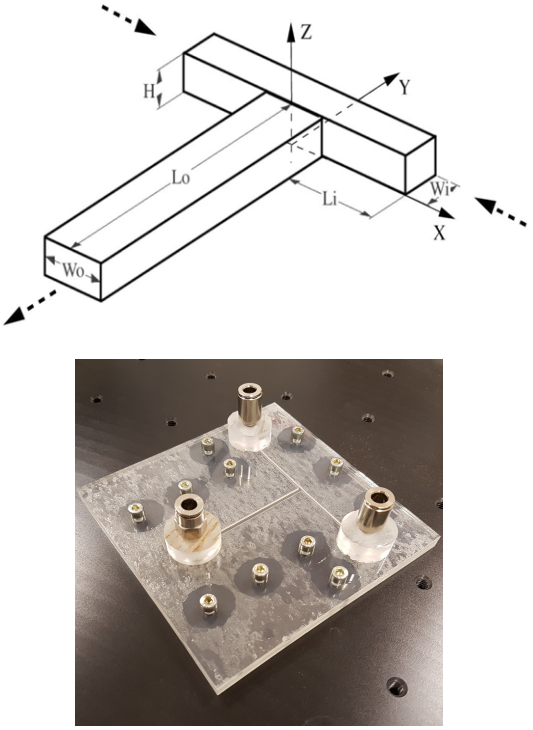

Figure 1: (a) T-mixer geometry; (b) experimental model.

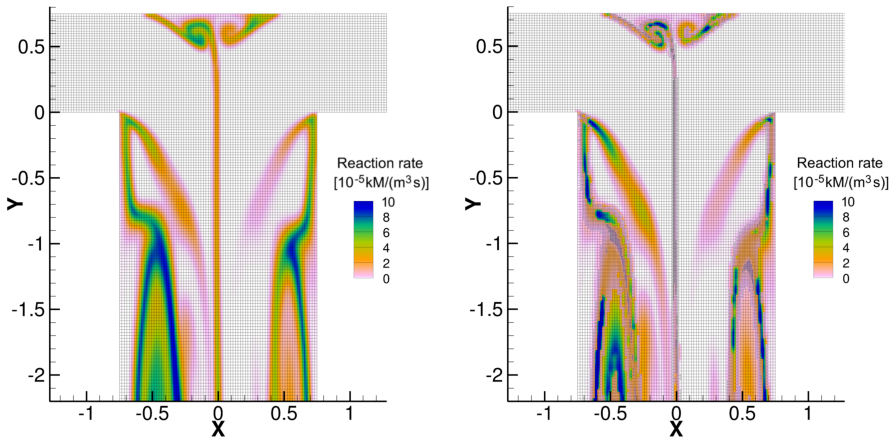

Figure 2: Details of (a) original and (b) adapted grid. Colors represents reaction rates.

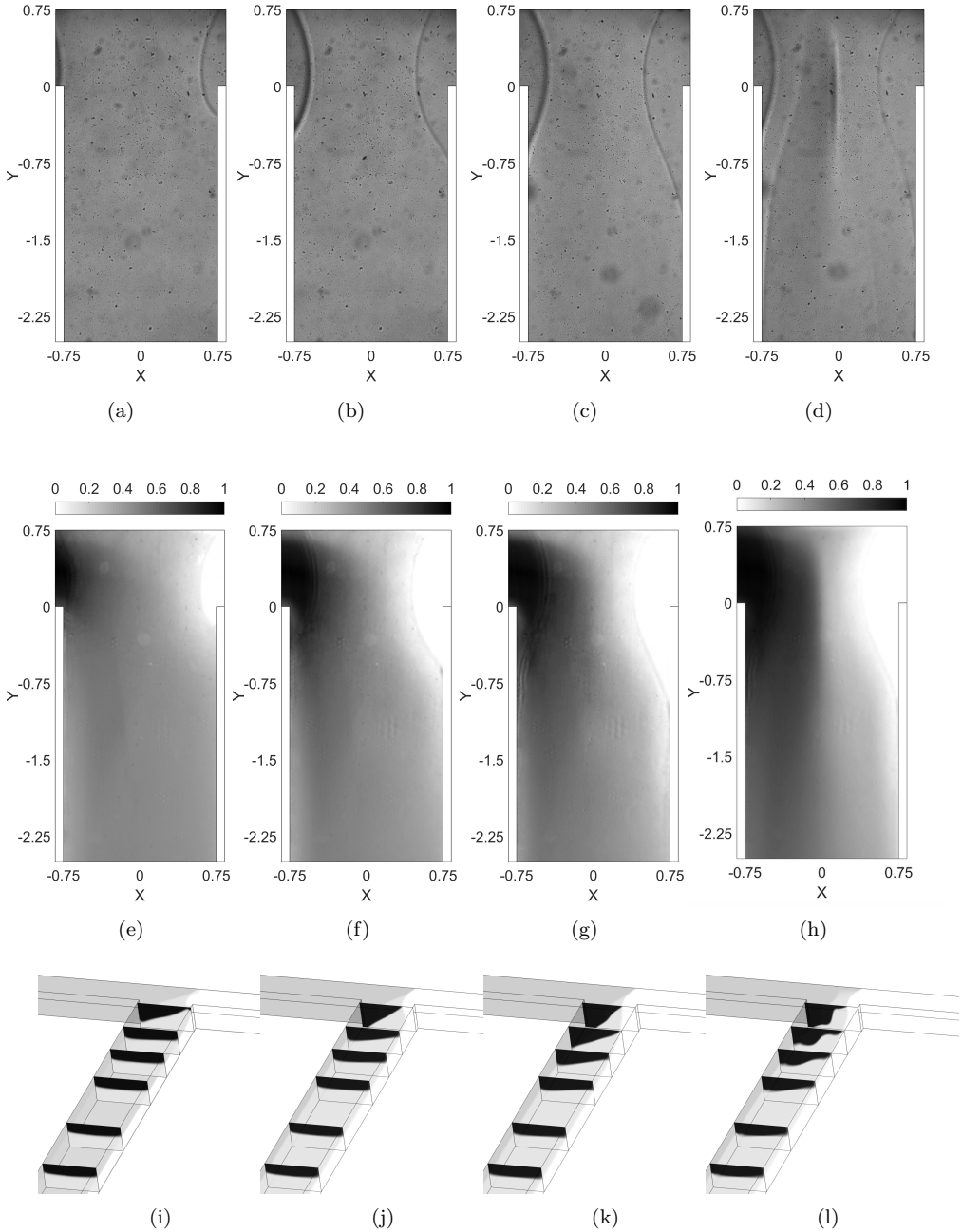

Figure 3: Results for [HCl] = 1.00 mol/L (test n. 2). Reynolds number (from left to right) $Re = 10, 20, 30, 60$. Experimental flow visualizations (a−d), experimental non-dimensional depth-averaged MB^+ concentration (e−h) and numerical non-dimensional MB^+ concentration in different cross-sections of the mixing channel for $-20 \leq Y \leq -0.5$ (i−l).

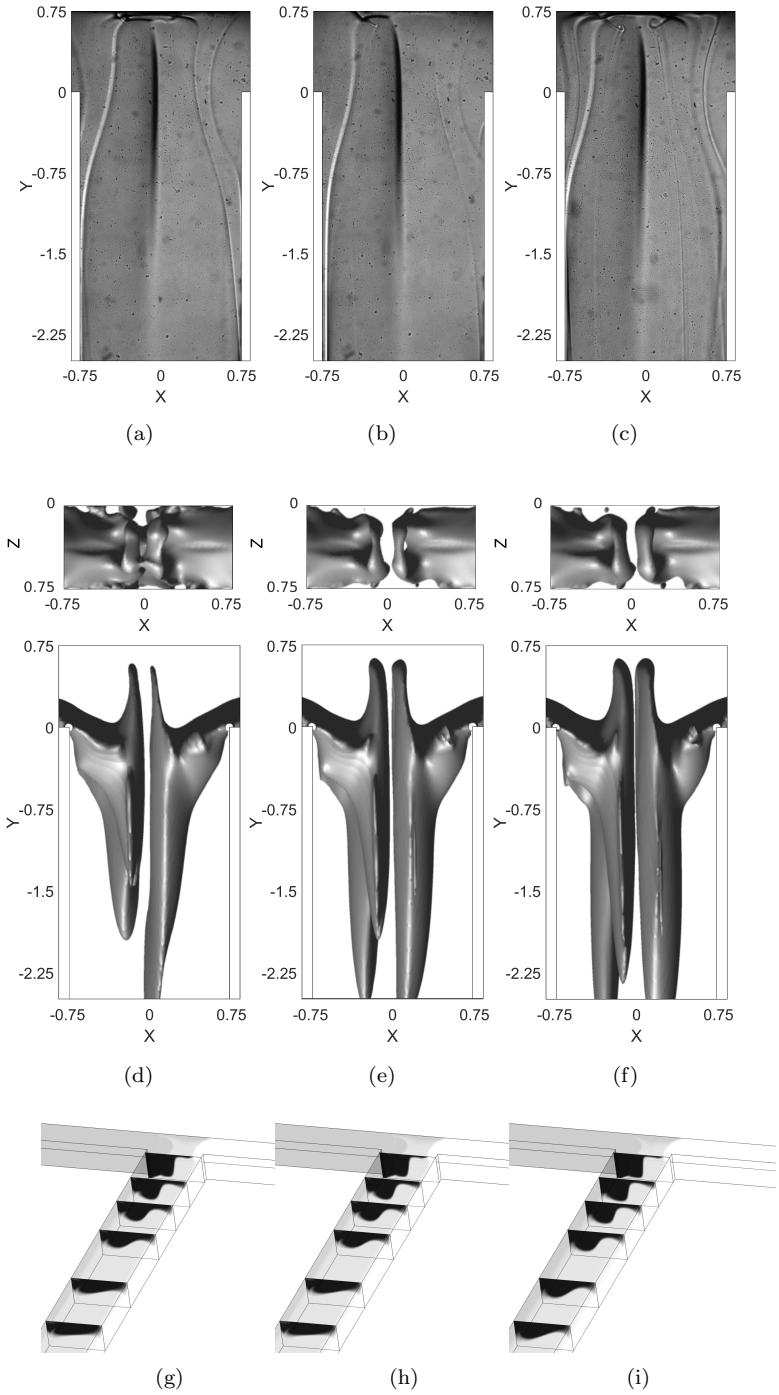

Figure 4: Results for [HCl] = 1.0 mol/L (test n. 2). Reynolds number (from left to right) $Re = 80, 100, 120$. Experimental flow visualizations (a−c), numerical iso-surface of the vortex indicator λ_2 (d−f) and non-dimensional MB^+ concentration in different cross-sections of the mixing channel for $-20 \leq Y \leq -0.5$ (g−i).

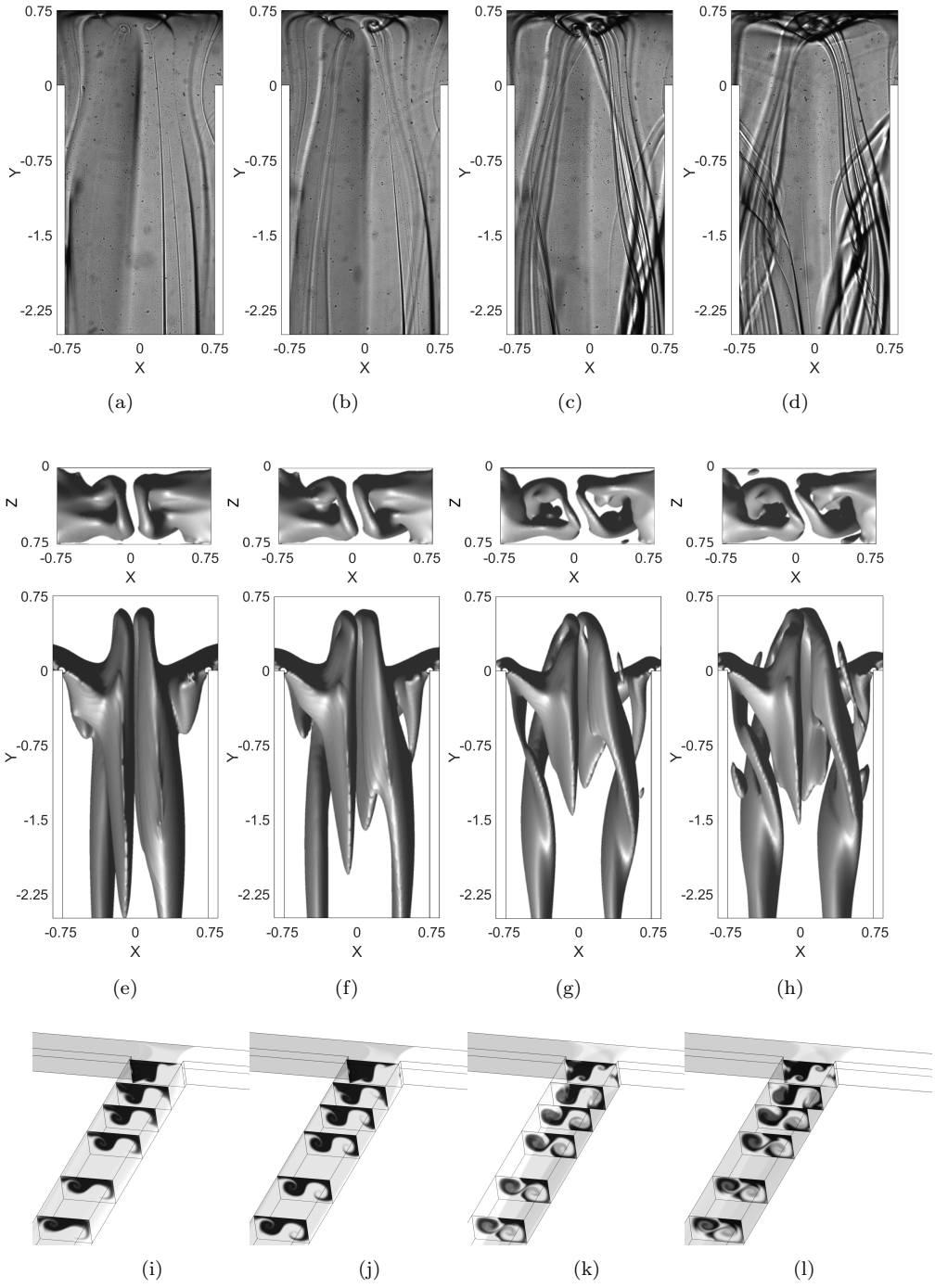

Figure 5: Results for [HCl] = 1.00 mol/L (test n. 2). Reynolds number (from left to right) $Re = 150, 180, 230, 280$. Experimental flow visualizations (a−d), numerical iso-surface of the vortex indicator λ_2 (e−h) and non-dimensional MB^+ concentration in different cross-sections of the mixing channel for $-20 \leq Y \leq -0.5$ (i−l).

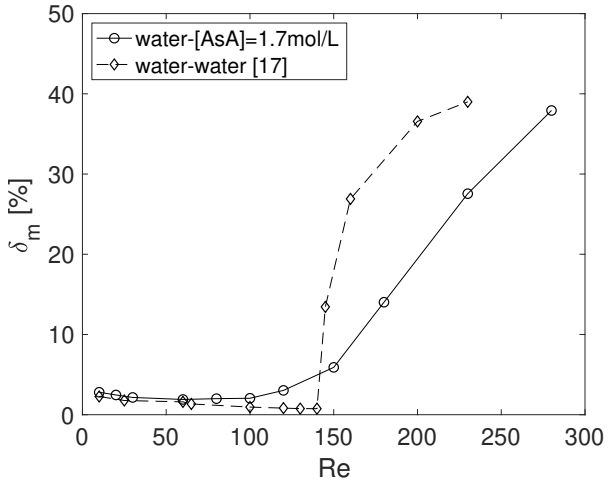

Figure 6: Mixing degree in the $Y = -25$ cross-section of the mixing channel as a function of the Reynolds number.

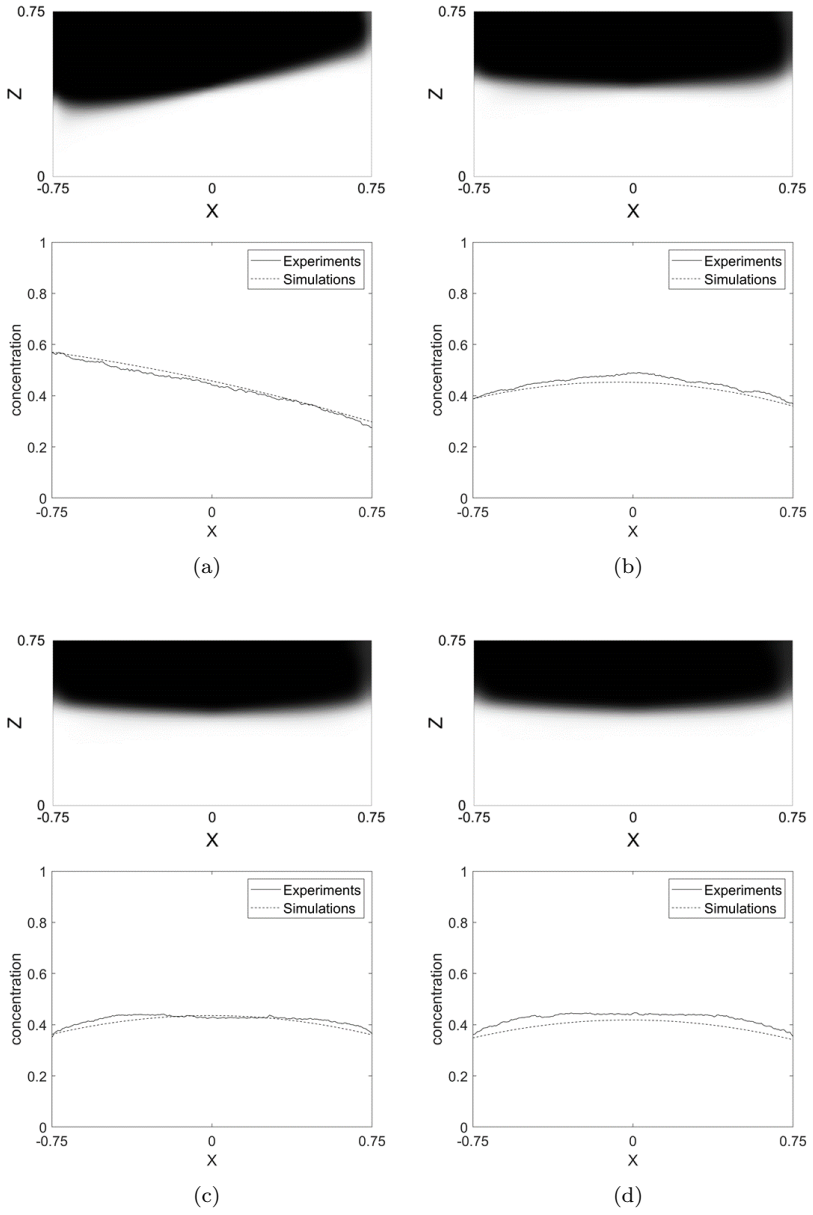

Figure 7: Non-dimensional MB^+ distribution predicted through numerical simulations (top) and comparison between experimental and numerical non-dimensional depth-averaged MB^+ concentration (bottom) for $Re = 30$ and [HCl] = 1.00 mol/L at different cross-sections in the mixing channel: (a) $Y = -2$; (b) $Y = -7.5$; (c) $Y = -15$; (d) $Y = -25$.

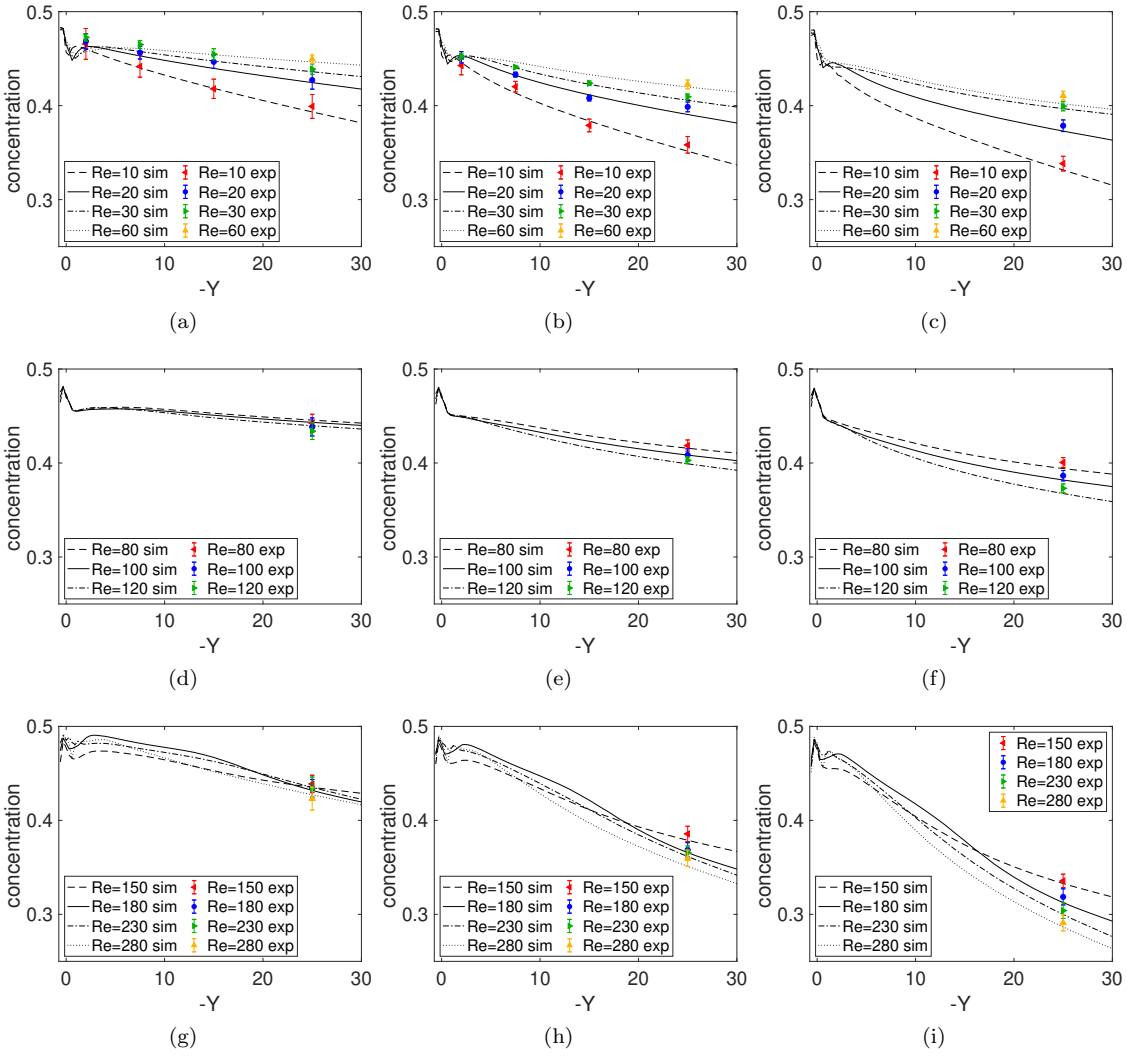

Figure 8: Comparison between experimental and numerical non-dimensional MB^+ concentration along the mixing channel for (a,d,g) [HCl] = 0.10 mol/L, (b,e,h) [HCl] = 1.00 mol/L, (c,f,i) [HCl] = 2.19 mol/L and for different Reynolds numbers corresponding to (a,b,c) the stratified regime, (d,e,f) the vortex regime and (g,h,i) the engulfment regime.

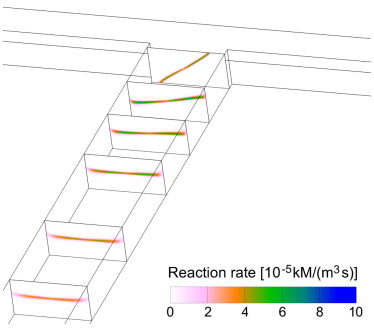

(a)

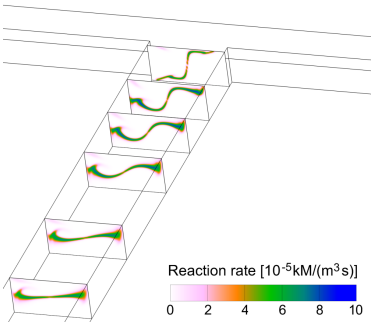

(b)

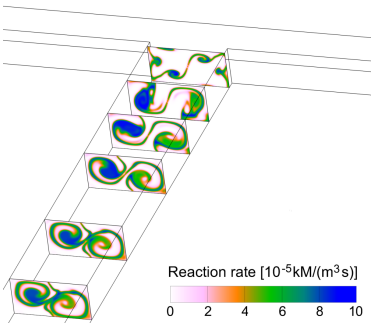

(c)

Figure 9: Reaction rate in different cross-sections of the mixing channel for $-20 \leq Y \leq -0.5$ (i–l) at: $Re = 20$ (a), $Re = 100$ (b), $Re = 230$ (c).

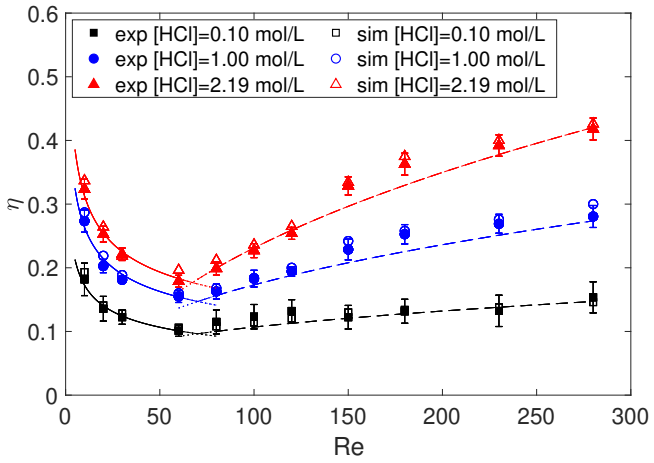

(a)

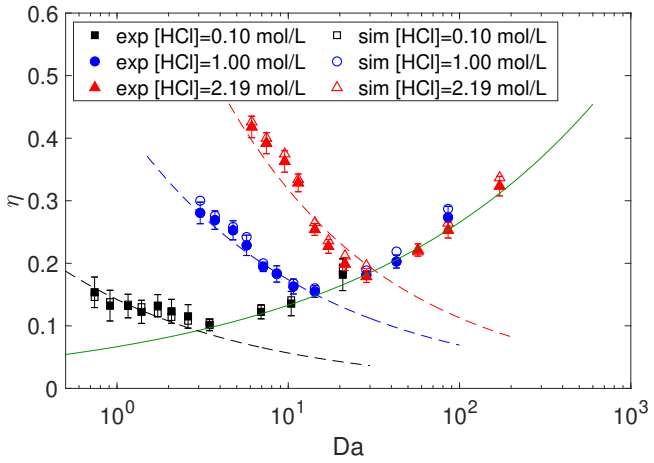

(b)

Figure 10: Experimental and numerical reaction yield at the $Y = -25$ cross-section of the mixing channel as a function of the (a) Reynolds and (b) Damkhöler numbers. Lines represent Eq. 13 and Eq. 14

List of Tables

Test	[mol/L]	k_r [1/s]
1	0.10	2.60
2	1.00	10.71
3	2.19	21.43

Table 1: Concentrations of HCl used in the experimental investigations and corresponding kinetic constants of the pseudo-first order reaction.

Grid refinement	1	2	3	4	Experiments
$Re = 100$	0.399	0.404	0.408	0.408	0.408 ± 0.007
$Re = 180$	0.357	0.362	0.366	0.368	0.369 ± 0.008
$Re = 280$	0.343	0.346	0.350	0.351	0.359 ± 0.009

Table 2: Non-dimensional average MB^+ concentration at the $Y = -25$ cross-section of the mixing channel as a function of the grid adaption cycles for different Reynolds numbers; [HCl] = 1.00 mol/L.